Gas-phase deposited nanolayers guard organic microparticles in polymer matrices for active corrosion protection at damages

Zhao, Jingjing; van Ommen, J. Ruud; Garcia, Santiago J.

DOI
10.1016/j.porgcoat.2024.108522

Publication date
2024

Document Version
Final published version

Published in
Progress in Organic Coatings

Progress in Organic Coatings 192 (2024) 108522

Contents lists available at ScienceDirect

Progress in Organic Coatings

journal homepage: www.elsevier.com/locate/porgcoat

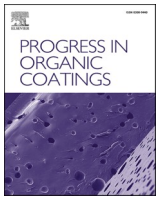

Gas-phase deposited nanolayers guard organic microparticles in polymer matrices for active corrosion protection at damages

Jingjing Zhao [a,*], J. Ruud van Ommen [b], Santiago J. Garcia [a,*]

[a] Aerospace Structures and Materials department, Faculty of Aerospace Engineering, Delft University of Technology, Kluyverweg 1, 2629 HS Delft, the Netherlands
[b] Department of Chemical Engineering, Delft University of Technology, 2629HZ Delft, the Netherlands

ARTICLE INFO

Keywords:
Chemical vapor deposition
Atomic layer deposition
Organic corrosion inhibitor
Self-healing
Functional particles

ABSTRACT

The most common way to protect metallic structures from corrosion is through the use of passive and active corrosion protection with coatings containing dispersed corrosion inhibitor particles. Current approaches use inorganic microparticles containing mostly toxic and/or critical elements (e.g. CrVI, Li-salts). Organic inhibitors have been identified as a potential replacement technology due to their high inhibiting efficiency in solution, high versatility and lower toxicity. Nevertheless, when brought into organic coatings these inhibitors lose their efficiency due to unwanted side reactions with the surrounding organic matrix (coating). In this work we propose a novel strategy to isolate the organic corrosion inhibitor microparticles from the surrounding matrix. The new approach is based on the gas-deposition of an oxide nanolayer on the microparticles using gas deposition in a fluidized bed reactor. As a result, the organic particles are better dispersed in the coating and do not react with the surrounding matrix. Upon coating damage the particles are exposed to water and release sufficiently high amounts of the organic corrosion inhibitor at the damaged location. The work introduces a technique that can be used in other applications with similar challenges and a new technology that enables for the first time to store large amounts of active organic corrosion inhibitors in reactive organic coatings for efficient protection of metallic infrastructure. This opens the path to the practical use of highly efficient organic inhibitors in coatings for corrosion protection.

1. Introduction

The need to replace highly toxic corrosion inhibitors in coatings has become widely acknowledged, representing a complex and multi-dimensional challenge. Organic corrosion inhibitor complexes and salts such as 2,5-Dimercapto-1,3,4-thiadiazole (DMTD) are considered promising alternatives to toxic Cr(VI)-based inhibitor salts and Lithium and Rare Earth salt alternatives because of their comparable intrinsic corrosion inhibition efficiency in solution, surface stability, reduced environmental impact, low molecular weight and design versatility. [1,2] Unfortunately, the efficient incorporation of organic inhibitors in organic coatings in sufficiently large amounts and without unwanted inhibitor-polymer matrix reactions has been so far largely elusive. As a result of matrix-inhibitor reactions, the coating properties are negatively affected and/or the inhibitors cannot be released from the coating to protect the underlying metal from corrosion, hence resulting in under-performance. [3,4] The hygroscopic, powder state and highly reactive nature of most good performing organic inhibitors limit the use of emulsion encapsulation techniques used in liquid encapsulation for self-healing coatings. [5] Alternative encapsulation strategies using nano [6–8] or micro [9–11] inorganic particles as carriers have been proposed and shown to be successful up to a certain point. These approaches allow the introduction of relatively low amounts of organic inhibitors in coatings and control their release by different mechanisms such as water dissolution and diffusion, pH or ion exchange but offer limited amounts of inhibitor locally. [10] In this work, we introduce the use of gas-phase deposition in a fluidized bed as a new strategy to embed large amounts of unreacted corrosion inhibitor microparticles in organic coatings through the use of a protective thin metal oxide nano-layer.

Gas-phase deposition methods such as (pulsed) chemical vapor deposition (CVD) and atomic layer deposition (ALD) are used to create non-selective homogeneous nanometer-thick (oxide) layers on flat, porous and regular substrates used mostly in electronic devices. [12–14] The introduction of gas-phase deposition in fluidized beds has recently allowed extrapolating the concept of thin layer deposition to micro-particles relevant for the pharmaceutical sector. In particular, layers of

* Corresponding authors.
E-mail addresses: J.Zhao-6@tudelft.nl (J. Zhao), S.J.GarciaEspallargas@tudelft.nl (S.J. Garcia).

https://doi.org/10.1016/j.porgcoat.2024.108522
Received 19 March 2024; Received in revised form 6 May 2024; Accepted 11 May 2024
Available online 17 May 2024

Al_2O_3, TiO_2 and SiO_2 have been applied as nanoscale thin films on organic drug particles via atomic layer deposition in fluidized bed reactors in order to control the particle dissolution rate in solution. [15–19] Besides controlling the drug release kinetics, such nanolayers on drug microparticles have been used to tune the surface chemistry to improve their dispersibility, flowability, and stability. [18–21] Organic corrosion inhibitors, share some properties with drug microparticles regarding moisture sensitivity (hygroscopic, solubility), and adhesive and cohesive character, but also tend to have more irregular shapes and broad particle size distributions affecting the local surface energy levels relevant to initiate gas-phase deposition. These factors leading to reduced flowing, increased agglomeration and formation of irregular layers increase the challenge in gas-phase fluidized bed deposition on reactive particles such as corrosion inhibitors and make developments non-obvious. Moreover, corrosion inhibitors are to be dispersed in organic matrices in an isolated form to prevent minimal negative side reactions but at the same time remain accessible to water ingress so that the inhibitors can be dissolved, transported and released rapidly at sufficiently large quantities from the coating (within 30 s for the case of aerospace alloys as AA2024-T3) [22] and sustained in time in order to protect the underlying metallic structure from corrosion and ultimate mechanical failure. This work explores for the first time these aspects using gas-phase deposition in the context of anticorrosive coatings.

To proof the concept, we use pulsed gas-phase deposition in a fluidized bed to deposit a TiO_x nanoscale layer on a selected model organic inhibitor (2,5-dimercapto-1,3,4-thiadiazole, DMTD) at 40 °C and atmospheric pressure (1 bar). The modified organic inhibitor particles are then incorporated in a solvent borne epoxy-amine coating and applied on an aerospace-grade aluminum alloy AA2024-T3 to test corrosion performance. The fluidized bed reactor provides good mixing between gas and solid phases, which benefits depositing a conformal titanium oxide layer. The deposition layer was studied by transmission electron microscopy (TEM), X-ray photoelectron spectroscopy (XPS) and in-situ ultraviolet-visible spectroscopy (UV–vis). The effect of the titanium oxide layer on the interaction between DMTD and epoxy-amine matrix was studied by thermogravimetric analysis (TGA), differential scanning calorimetry (DSC) and release kinetics using ex-situ UV–Vis. The impact of the nanolayer formed around DMTD microparticles on the active corrosion protection at damaged coatings (1 mm diameter damages) was evaluated under wet/dry cyclic exposure using in-situ highly resolved image reflectometry with image correlation and electrochemical potential noise measurements. The results allow presenting gas-phase deposition in a fluidized bed as a promising strategy to efficiently introduce large amounts of very reactive organic corrosion inhibitors in coatings and opens the path to the use of so far elusive functional chemicals in coatings and other polymeric matrices.

2. Experimental section

2.1. Materials

2,5-dimercapto-1,3,4-thiadiazolate (DMTD >99 %) particles were purchased from Sigma-Aldrich and used as substrates for the deposition. The precursor, titanium tetrachloride ($TiCl_4$) was purchased from Strem Chemicals and used as received. The demineralized water was used as a co-reactant with $TiCl_4$. Commercial grade bare 2.5 mm thick AA2024-T3 were cut into 10 cm × 10 cm pieces and used as metal substrates for coatings. Commercially available bisphenol-A based epoxy resin (Epikote™ 828) and amine crosslinker (Ancamine®2500) were supplied by AkzoNobel (NL) and used as-received to form the coating binder using xylene (99 %) as solvent. Sodium chloride (NaCl, >98 %) was purchased from VWR Chemicals. Milipore® filtered water was employed in all steps requiring water.

2.2. Gas-phase deposition experiments

The gas-phase deposition experiments were carried out in a vibrated fluidized-bed reactor operating at atmospheric pressure, as has been described in previous works. [16,17,19] DMTD powders were prepared by hand-milling and sieving under 120 μm. Before deposition, a fluidization test on DMTD particles was applied. N_2 (99.999 v/v%) was used as the carrier and purging gas. As a result, it was found that a maximum of 10 g DMTD (around 1/10 bed height) could be well-fluidized under 5 L/min nitrogen flow on a vibration table. Based on the fluidization test and the experience of earlier works [16,17], it was decided to use 0.5 L/min of precursor and co-reactant vapor with 4.5 L/min of nitrogen to keep the constant gas velocity in the whole reactor. Prior to the injection and fluidization of the DMTD, the reactor was heated up to 40 °C and kept at constant with the help of a heating jacket wrapped around the glass column. The precursor, $TiCl_4$, and the co-reactant, H_2O, stored in bubblers were fed to the reactor through separate inlet tubing. The stainless-steel tubing that connects the bubblers to the reactor was maintained at 30 °C above the bubblers at room temperature to prevent the precursor from condensing. The deposition process consisted of sequential exposures of the DMTD to $TiCl_4$ for 45 s, 5 min purging with only nitrogen gas, and H_2O for 60s (one cycle) followed by another 5 min nitrogen gas purging step prior to the next cycle of exposure to precursor and co-reactant. The exposure time to $TiCl_4$ and H_2O were chosen based on the experience of earlier works using also cohesive but nano-sized particles, allowing sufficient exposure time [16,17]. The purge time of 5 min allows for any excess reactants or by-products to be cleared from the system before a subsequent cycle begins. The reaction: $TiCl_4 + H_2O \rightarrow TiO_x + HCl$ allowed for the deposition of a Ti oxide layer on the DMTD microparticles. The by-product, HCl, was neutralized by 1 % NaOH solution in the wash bottle connected to the outlet of the reactor. The gas-phase depositions of TiO_x were run for 20, 30, 40, 50, and 60 cycles. To get an impression of the effect of the fluidization on the particle size distribution, a test was performed doing 20 cycles without precursor and co-reactant.

2.3. Particles characterization

The images of the gas-phase deposited DMTD particles were taken by Keyence Laser Scanning Confocal Microscope and used to evaluate the particle size distribution with the ImageJ software, according to the following protocol: (1) Calibrating the image scales (pixels- > microns) in Image J by the function of “setting scale”; (2) The threshold of each image is adjusted (150 to 255); (3) The particles are analyzed by the function of “Analyze particles”, to give the area of each particle; (4) All the particles are assumed as circles to get the diameters; (5) Finally, we plot the histogram of all the diameters to get the particle size distribution. The presence of the deposition layer on DMTD was assessed by transmission electron microscopy (TEM) and X-ray photoelectron spectroscopy (XPS). In TEM, the samples were dispersed in Hexane and drop cast into a C foil supported with a Cu grid. The particles were very beam sensitive so only low magnification (~100kx) could be used. The XPS was equipped with a monochromatic Al anode X-ray source with a spot size of 400 μm. The photo-electrons are detected by a 128-channel detector, with a 0.1 eV resolution. For survey spectra, the pass energy and step size were set to 140 eV and 0.40 eV respectively. High-resolution spectra were obtained with 50 eV pass energy and 0.1 eV resolution. All spectra were calibrated by assigning the true energy value (284.8 eV) corresponding to the position of a C 1s peak. The dissolution kinetics of DMTD/TiO_x particles in real time was studied with a PerkinElmer LAMBDA 35 UV/VIS spectrometer operated at a constant wavelength representative of the DMTD inhibitor presence in NaCl solution (i.e., 328 nm). This allowed a scan rate of one measurement per second during the 2 h duration of the release tests. A calibration curve made with DMTD solutions (see supporting information Fig. S1) was used to convert absorption intensity of the representative wavelength to

inhibitor concentration in solution. To this aim the powders (inhibitors) were placed inside a Whatman® grade 1 paper filter on top of a UV cuvette filled with 0.05 M NaCl solution. As seen in Fig. S1.b, release of the inhibitor was captured short after immersion as a result of inhibitor dissolution. In order to ensure an even DMTD dispersion in the cuvette and to avoid false measurements the solution was constantly magnetically stirred at 1600 rpm.

2.4. Coatings preparation

The 2.5 mm thick AA2024-T3 metal sheets were cut into pieces of 100 × 100 mm prior to surface cleaning and coating application. The surface cleaning consists of the following steps: (1) removal of the native oxide layer and surface roughness formation by Scotch Brite 3 M; (2) degreasing with acetone;(3) pseudo-boehmite treatment on the coupons to increase the amount of reactive hydroxyl groups on the surface by 10 s immersion in 2 M NaOH followed by a 30 s immersion in distilled water and drying with nitrogen.

Three different coating compositions are prepared as listed in Table 1. Different inhibitor pigments are added to the identical coating binder formulation. The coatings formulation is given as a function of epoxy resin (phr = parts per hundred epoxy resin in weight). Briefly, Epikote™ 828, Ancamine®2500 and xylene (weight ratio 2.70:1.57:1.06) were mixed for 5 min in a high-speed mixer at 2500 rpm and pre-cure at room temperature for 15 min. After adding the inhibitor pigments, the coating formulation was manually stirred and applied onto the Teflon sheets for thermal analysis and metal coupons for release and corrosion tests using a doctor blade with a wet thickness of 100 μm. After a flash-off period of 30 min the coatings were cured at 60 °C for 24 h. The samples were stored in a desiccator before the following tests.

2.5. Thermal analysis

The coatings applied on Teflon sheets were separated by a spatula and used for thermal analysis. The thermal degradation of the coatings as a function of adding different inhibitor pigments was analyzed by Thermogravimetric analysis (TGA). The TGA tests were conducted from 30 °C to 600 °C at a rate of 10 °C/min under nitrogen gas with a flow rate of 20 mL/min. Differential scanning calorimetry (DSC) analyses were performed to investigate the TiO_x layer influence on the cross-linking density of the epoxy/amine coating systems. DSC tests were carried out via a TA Instr. Modulated DSC under nitrogen flow. Each sample was heated at a temperature range from −10 °C to 80 °C at a heating rate of 10 °C/min. The DSC provides information on the glass transition temperature (T_g) of the coatings.

2.6. Inhibitor release tests from coatings

The coating systems with DMTD and DMTD/TiO_x applied on AA2024-T3 in Table 1 were surface ground by 1000-grit paper during 15 s, followed by exposure to 40 mL 0.05 M NaCl solution. This allowed direct exposure of the particles to the electrolyte by removing the top polymeric thin layer on the coating. The diameter of the circular exposed ground area is 1 cm. Samples of 3 mL were collected at different time points (1, 5, 15, 30, 60, 120, 240, 360, 1440, 2880, and 4320 min) and put back after each measurement to maintain a constant volume of release medium. The aliquots were tested in a UV–Vis spectrometer using a wavelength range from 700 nm to 200 nm. The absorbance at characteristic peak location of 328 nm was used to obtain the inhibitor concentration using the calibration curve in Supporting information Fig. S1.

2.7. Wet/dry cyclic exposure tests

A Roland EGX-350 engraver equipped with an end mill carbide tip of 1 mm in diameter was used to create circular damage on the coated panel surface prior to immersion in electrolyte for the corrosion studies. Drills of 1 mm wide and 0.25 mm deep (i.e. well into the metallic substrate) with respect to the coated surface were created without delamination. The resulting chips from the engraved zone were removed by air blowing. The corrosion was evaluated with an in-situ optical electrochemical set-up as we described in previous works. [10,22] The scribed coating sample was mounted in a magnetic Raman electrochemical flow cell from Redox.me. This cell allows a total electrolyte volume of 4.5 mL and the use of a small Ag/AgCl (3 M KCl) reference electrode. The electrochemical cell was placed vertically in a Faraday cage on an optical table from ThorLabs to avoid any electromagnetic and vibrational disturbances. The EPN signals are recorded with an Ivium Compactstat controlled by IviumSoft V2.86. The maximum range of the potentiometer was set at ±1 V vs Ag/AgCl. The interval time between data points was set to 0.05 s (sampling frequency of 20 Hz) combined with a low-pass filter of 10 Hz. A Dino-Lite digital microscope was placed at the window side of the electrochemical cell. This allows obtaining high-resolution images every minute during exposure simultaneously to the Electrochemical potential noise (EPN) measurements as a function of the exposure time. Due to the 8-led ring light type of the microscope and the high roughness of the damage left by the engraver, the lightness of the images is not even on the damage (shadow can be seen). To eliminate the shadow, a coaxial light cap was equipped. The shadow was still not completely removed but mostly avoided. This will be further improved in future works. The electrolyte (0.05 M NaCl solution) was injected through side openings allowing the capturing of optical and electrochemical information right after exposure to the electrolyte. The optical analysis was conducted in ImageJ software as described in earlier works. [10,22] The technique is based on a pixel-by-pixel analysis of the progression of surface activity on the region of interest (ROI) over time. Images were converted to grey scale at an 8-bit resolution allowing the definition of 256 different levels of intensity between black and white. For both the exposed metal surface, i.e., damage and the surrounding coating, a static thresholding bin limit of 10 was used due to the small intensity changes.

The wet/dry cyclic exposure tests were performed to study the active corrosion protection by inhibitors released from the coating to the scribed site under discontinuous immersion conditions. The tests consist of a process of 2 h exposure of damaged coating in 0.05 M NaCl solution and monitored by the above optical-electrochemical set-up. And then, the coating was taken out followed by gentle flashing in demineralized water, dry in N_2, and placed in an ambient environment for 1 h. The coating was put back into the same set-up and started over the new cycles. In total, we performed 1 cycle on Epoxy coating without inhibitors, 3 cycles on Epoxy-DMTD coating and 3 cycles on Epoxy-DMTD/TiO_x coating. After each cycle, the solutions were collected and used to obtain the inhibitor concentration in the same manner as explained in 2.6. The concentrations of DMTD released from a coating

Table 1
Coatings formulations as a function of Epikote™ 828 (phr = parts per hundred epoxy resin in weight), and the calculated inhibiting active component in wt% of the total coating dry weight and pigment volume concentration (PVC%) of inhibitor pigment. The weight of TiO_x was ignored.

Sample name	Inhibitor pigment	Inhibitor (phr)	Inhibiting active component (wt%)	PVC (%)	Dry coating thickness (μm)
Epoxy	–	0	0	0	68 ± 3
Epoxy-DMTD	DMTD	25	13.7	10	70 ± 3
Epoxy-DMTD/TiO_x	DMTD/TiO_x 20 cycles	25	13.7	10	70 ± 3

without damage were also measured under the same conditions of exposure. To calculate the amount of DMTD released specifically due to the damage, the amount released from the damaged coating was subtracted from the amount that could have been released from the same area of the intact coating.

3. Results and discussion

3.1. Gas-phase deposition of protective nanolayer on organic inhibitor microparticles

Fig. 1a shows the negative effect of organic corrosion inhibitor microparticles (2,5-dimercapto-1,3,4-thiadiazole, DMTD) directly added into a chemically reactive epoxy-amine polymer network. In such polymers, the crosslinking process proceeds through nucleophilic attack of the amine on the oxirane groups leading to ring opening and a reticulated (crosslinked) polymer network. [23,24] In this environment, the thiol groups (-SH) in the DMTD organic molecule are deprotonated by the base amino groups to create highly nucleophilic thiolates (—S—) able to ring open the oxirane groups and disturb the crosslinking process through the formation of linear chains. [25] Such side chemical reactions ultimately affect the polymer properties (e.g. glass-transition temperature, Young's Modulus, Stress at break, adhesion) but also the release potential of the corrosion inhibitors at damaged locations upon exposure to a corrosive electrolyte (e.g. NaCl solution). To prevent this negative reaction a TiO_x (titanium oxide) nanolayer was deposited on the microparticles using a pulsed-chemical vapor deposition (CVD) process in a sequential approach as done in atomic layer deposition (ALD) processes. Fig. 1b shows a schematic of the CVD process in a fluidized bed reactor used in this work as explained in the Experimental section and Supporting Information in detail. In this process, the particles are fluidized ("floating") in N_2 and the chemical reactants are sequentially added to the fluidized particles with the N_2 flow. For the proof of concept shown in this work, $TiCl_4$ was used as the precursor to create the nanolayer. The precursor was chosen in order to obtain a nanolayer (i.e. TiO_x) able to first impede the reaction with the surrounding polymer matrix but then allow for inhibitor release through solubility in water. As the TEM-EDX images in Fig. 1b show, when 20 cycles were used, a TiO_x nanolayer of 20 to 30 nm was deposited on the surface of the organic microparticle. The immediate positive effect of the protective nanolayer (20 cycles) on the DMTD microparticles compatibility with the epoxy-amine polymer matrix can be seen in Fig. 1c, where the nanolayer led to an improved degree of particle dispersion as seen by the absence of the agglomerates visible in Fig. 1a, and the uniform orange-like coloration associated with DMTD microparticles.

Fig. 2 shows TEM-EDX mappings of DMTD/TiO_x particles, the presence of TiO_x layers on DMTD surface and Ti atomic percentage increasing with deposition cycles. The TEM-EDX images show the efficient deposition of a 20–30 nm TiO_x layer on the inhibitor microparticle (identified with the S marker) after 20 cycles. This suggests the nanolayers were formed through a chemical vapor deposition (CVD) process rather than atomic layer deposition (ALD) despite an alternating supply of the gas phase reactants with N_2 purging in between was used instead of continuous reactant supply without purge. As a result of a non-optimized process, the fluidized bed reactor was operated at low temperature, which allows excess amounts of reactants ($TiCl_4$ and H_2O) to adsorb onto hygroscopic DMTD surfaces and react during the subsequent reaction.

Fig. 3a shows the particle size distribution of the organic microparticles which did not change after 20 cycles gas phase deposition process. When more deposition cycles were employed (30 or 40 cycles), no significant differences in the nanolayer (Fig. 2a) and particle size distribution (2–8 μm) were found. Nevertheless, at 60 cycles, particle agglomeration resulted in an increased particle size and particle distribution (2–12 μm). This is attributed to the hygroscopic nature and low temperature used during the gas phase deposition process. The chemical compositions of DMTD/TiO_x particles were characterized by XPS. Supporting Information Fig. S2 shows the two peaks at around 458.5 eV and 464.5 eV reflect the doublet state of Ti2P (i.e., Ti 2p3/2 and Ti2p1/2) [26] although the oxidation states vary with cycle numbers, suggests the uneven growth of TiO_x especially at high cycle numbers, which is corresponding with the bigger particle size obtained at high cycle numbers from PSD analysis as shown in Fig. 3a. As seen in Fig. 3b, the normalized intensities of S2p and C1s peaks of the bound thiol (BE = 161.9 eV) increase while that of N=C-S bound (BE = 286.6 eV) decrease after deposition. [27] This suggests the formation of Ti-O(—Ti)-S at the interface between TiO_x and DMTD. Considering the limited detectable depth of XPS (5 nm), the thickness of the TiO_x layer might not be uniform across the DMTD particles. This possibility of the island growth is evidenced by our TEM-EDX results as shown in Fig. 1b in which islands are visible on the DMTD/TiO_x particles. Future research focuses on shell optimization should lead to strategies to avoid this phenomenon. Lower cycles (<10) were not investigated in this proof-of-concept work due to the observed limited effect of the number of cycles on the particle size distribution, nanolayer thickness, chemical composition, and dissolution kinetics of the microparticles (Supporting Information Fig. S1b) but

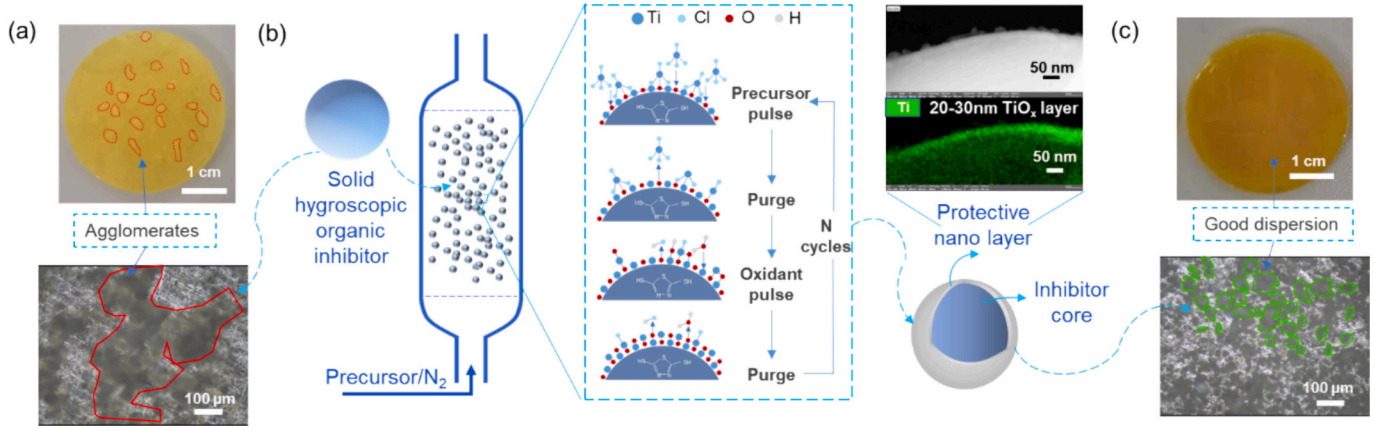

Fig. 1. (a) Micrographs show the poor dispersion of the organic (DMTD) microparticles in an organic (epoxy-amine) polymer network. The red lines in the micrographs indicate locations of inhibitor agglomerates resulting from the reaction between the organic particle and the surrounding matrix; (b) Schematic illustration of the gas-phase deposition process of a protective nanolayer on organic corrosion inhibitor microparticles in a fluidized bed reactor. Image inserts show TEM-EDX images of a 20-30 nm TiO_x nanolayer deposited on an organic corrosion inhibitor particle after 20 cycles; (c) Micrographs show how a deposited nanolayer around the organic particles improves the dispersion quality of the particles in an organic polymer network. The green lines in the bottom micrograph indicate the locations of some inhibitor particles. (For interpretation of the references to color in this figure legend, the reader is referred to the web version of this article.)

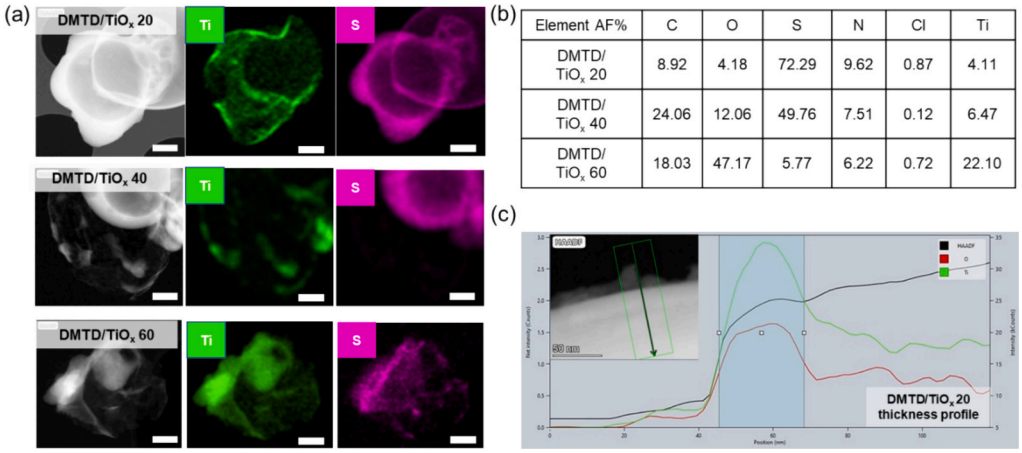

Element AF%	C	O	S	N	Cl	Ti
DMTD/ TiO_x 20	8.92	4.18	72.29	9.62	0.87	4.11
DMTD/ TiO_x 40	24.06	12.06	49.76	7.51	0.12	6.47
DMTD/ TiO_x 60	18.03	47.17	5.77	6.22	0.72	22.10

Fig. 2. (a) TEM-EDX mappings, (b) atomic elements compositions of DMTD/TiO_x particles at 20, 40 and 60 deposition cycles, and (c) thickness profile which is 20 to 30 nm of TiO_x 20 cycles layer on DMTD. Notes: DMTD particles are easily damaged under the electron beam of TEM which shows as "hollow" particles in EDX mappings. The scale bars in EDX are 500 nm. Mappings of S show the presence of DMTD particles. Mappings of Ti represent the success of TiO_x deposition.

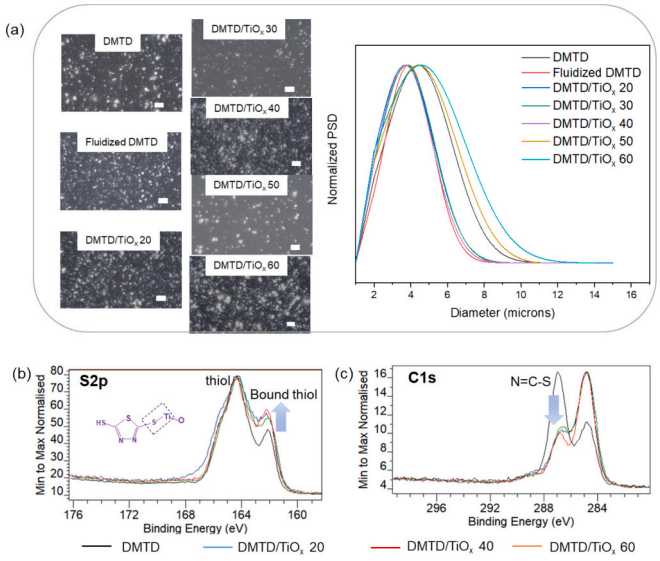

Fig. 3. (a) Confocal microscope images and particle size distributions of DMTD, fluidized DMTD, and gas-phase deposited DMTD particles at 20 to 60 cycles. Scale bar: 20 μm. And S2p (b) and C1s (c) XPS spectra of DMTD/TiO_x 20, DMTD/TiO_x 40, and DMTD/TiO_x 60 show the interaction of TiO_x depositions with S in the substrate.

will be objective of study in future works.

3.2. *Effect of protective nanolayer on inhibitor-organic coating interaction*

To further prove the benefit of the nanolayer around the organic inhibitor in reducing its interaction with the organic coating, thermal gravimetry analysis (TGA), differential scanning calorimetry (DSC), and Ultraviolet–visible spectroscopy (UV–Vis) analysis were performed in order to ascertain the effect on polymer film degradation (TGA), glass transition temperature (T_g) and inhibitor release kinetics.

As can be seen in Fig. 4a, the thermal degradation profile of the pristine epoxy coating can be differentiated into three stages: first stage (showing a drop followed by a pseudo-plateau up to 300 °C) with 20 % mass loss attributed to the loss of low molecular weight components; second stage (300-450 °C) with around 55 % mass loss attributed to the degradation of epoxy-amine crosslinking networks; and a third stage (above 450 °C) due to the carbonization of residuals. [28] When introducing unmodified DMTD into the epoxy coating, the onset degradation temperature of the Epoxy-DMTD coating was increased from 100 to 150 °C, suggesting that the excessive epoxy or/and amine monomers are stabilized by the reaction with DMTD in a thiolate-oxirane ring opening reaction process. However, the reaction between DMTD and the epoxy matrix also results in massive weight loss during first and second-stage degradations likely due to the expected weaker bond formation (S—C vs C—C) and lower crosslinking density. DSC analysis further supports this idea as the mid-point glass transition temperature (T_g) of the epoxy matrix decreased from 44 °C to 19 °C when the untreated DMTD particles were added to the epoxy-amine coating (Fig. 4b). A different effect is observed when the coated DMTD particles (DMTD/TiO_x particles) are used. In this case the coatings exhibit similar thermal stability as the pristine epoxy coating matrix. The only difference is the disappearance of the flat stability stage at 350 °C, which is attributed to the lower thermal stability of side DMTD-Epoxy groups compared to a full epoxy-amine network. In addition, compared to the pristine epoxy matrix, the glass transition temperature dropped from 44 ± 0.5 °C to 32 ± 0.5 °C. This shows still some reactivity probably due to non-perfect particle coverage, but 13 °C lower T_g drop than without the protective nanolayer, as seen in Fig. 4b. The results, even for these non-optimized systems, confirm the protective effect of the TiO_x nanolayer on DMTD leading to a reduced reactivity with the surrounding epoxy matrix and having a lower negative effect on the overall coating performance.

In order to study the effect of the TiO_x nanolayer on the availability of DMTD in the presence of water (release of DMTD from the polymer in an aqueous corrosive media), the surface of Epoxy-DMTD and Epoxy-DMTD/TiO_x coatings were ground with 1000 grid sanding paper, and exposed to 0.05 M NaCl solution for 3 days. This allowed direct exposure of the particles to the electrolyte by removing the top polymeric thin layer on the coating. UV–vis measurements of aliquots taken in time and the use of a calibration curve allowed quantifying the DMTD release in time. Fig. 4c illustrates the release profile and provides a schematic representation of water ingress and inhibitor release of these coatings. The Epoxy-DMTD/TiO_x coating shows higher inhibitor release over time compared to the Epoxy-DMTD coating, which is in agreement with the lower negative interaction between the DMTD and the coating matrix. It should be noted that, in anticorrosive coatings, an initial fast inhibitor release leading to a minimum local concentration able to protect the metal is needed since the initial dealloying of AA2024 happens within 5 min. [22] The desirable coatings therefore rely on a release profile that commences with an initial rapid release followed by a continuous long-term release. [10,29] For the Epoxy-DMTD/TiO_x coating, 50 % of the present DMTD can be released within the initial 2 h and is followed by a sustained (slower) release until plateau at 3 days exposure having reached 65 % release of the available DMTD. This can be attributed to

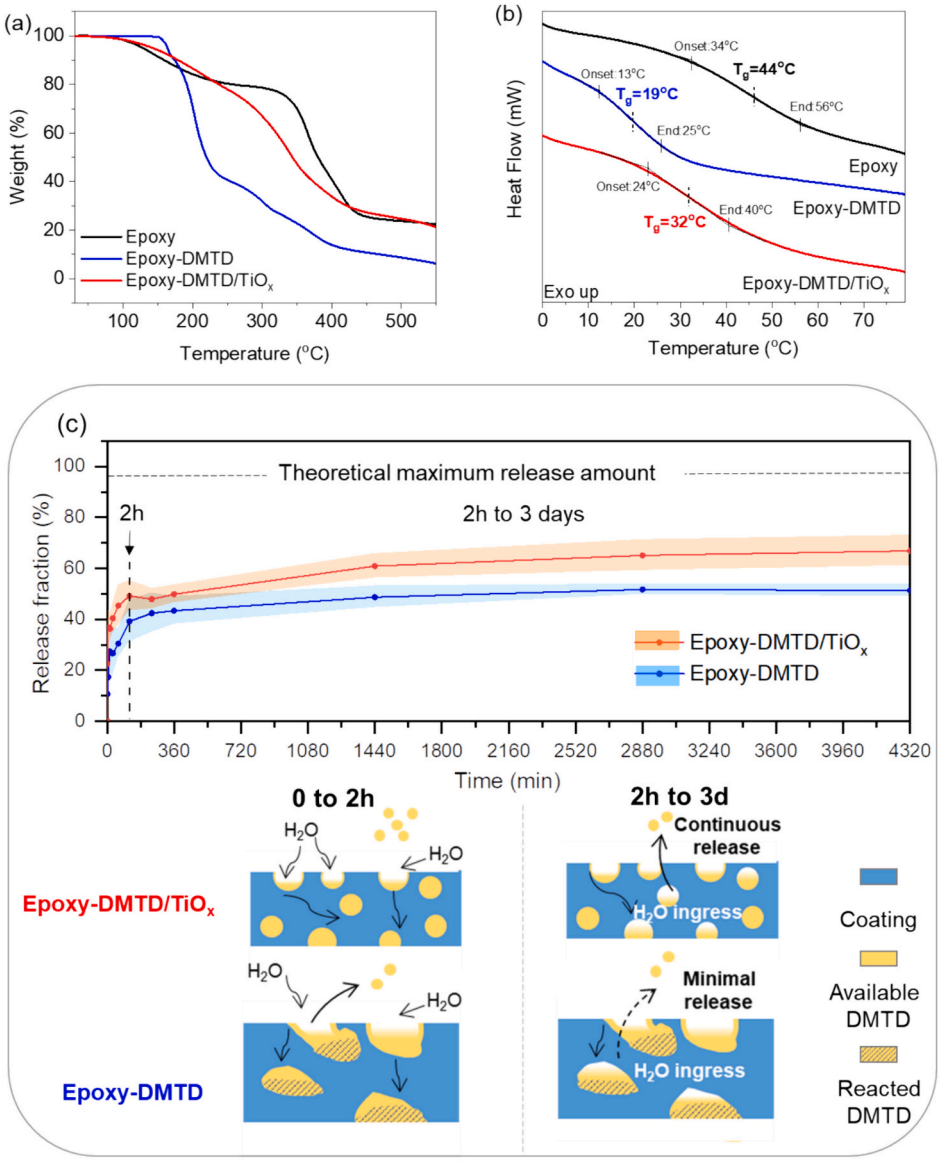

Fig. 4. (a) TGA and (b) DSC analysis of Epoxy, Epoxy-DMTD, Epoxy-DMTD/TiO_x coatings; (c) Release profile and schematic diagram of DMTD release from coatings exposed to 0.05 M NaCl solution over 3 days from Epoxy-DMTD and Epoxy-DMTD/TiO_x coatings. The release profile shows the average of several measurements (line) and the standard deviation (color band). The schematic diagram shows the cross-section of the coatings in two stages: the first stage from 0 to 2 h, representing a rapid initial release of the DMTD inhibitor, and the second stage from 2 h to 3 days, indicating a prolonged, long-term release in the case of Epoxy-DMTD/TiO_x samples.

the unavailability of the DMTD particles to water in relatively thick polymer films used in this test (70 ± 3 μm) but also to the partial reactivity between DMTD and the epoxy matrix indicated in Section 3.1. In contrast, the release of DMTD from the Epoxy-DMTD coating reaches a plateau at 40 % already within 2 h exposure to electrolyte. This lower release from the Epoxy-DMTD coating is attributed to the strong interaction between DMTD and the epoxy-amine matrix resulting from side reactions in absence of a protective nanolayer.

This effect becomes evident when analysing the polymers after exposure. In Fig. 5 it can be seen how the use of TiO_x nanolayers led to higher particle dispersion and a higher amount of smaller black dots related to holes created upon inhibitor dissolution, in good agreement with higher release fractions in Epoxy-DMTD/TiO_x coatings due to the TiO_x layer protection. While the Epoxy-DMTD/TiO_x coating does not reach the theoretical maximum release (98 % considering the TiO_x layer), it is still significantly higher than for Epoxy-DMTD coatings (65 % vs 40 %). In addition, the total releasing period increased from 2 h to 3 days when replacing pristine DMTD with DMTD/TiO_x, which is beneficial for protecting newly exposed areas and prolonging corrosion protection.

3.3. *Effect of protective nanolayer on active corrosion protection at damaged coatings under wet-dry cyclic exposure*

In an active anticorrosion coating system, it is generally accepted that the protection at corrosion-inhibited locations will be ultimately lost under more aggressive exposure conditions, such as wet-dry cyclic exposure. This decline in corrosion inhibiting power is generally related to a reduction in the inhibitor supply from the coating and indirectly implies that the created inhibiting layers may not be sufficiently stable or robust, thereby failing to guarantee prolonged protection of the metal without a constant supply of inhibitor. Even if the stability of inhibiting layers is a largely unexplored concept, it is now known that inhibitor layers created from 1 mM DMTD/0.05 M NaCl solutions on AA2024-T3

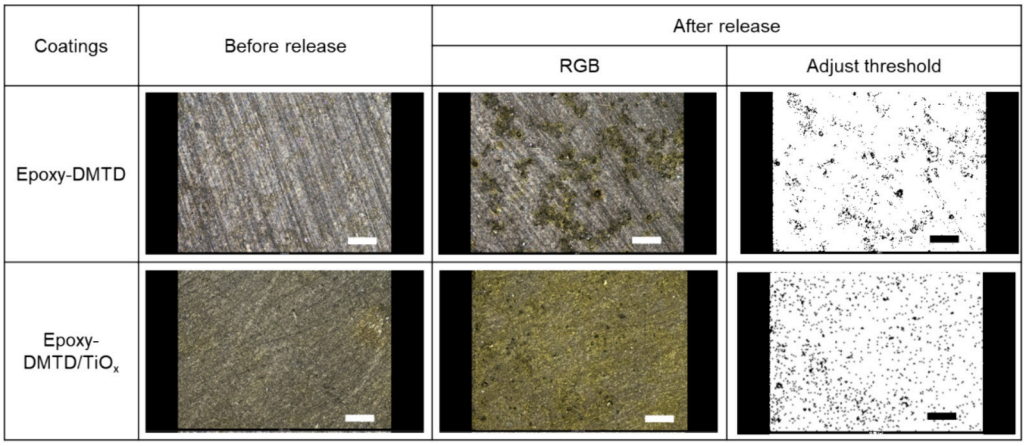

Fig. 5. The images of Epoxy-DMTD and Epoxy-DMTD/TiOx coatings before and after the release tests made by confocal microscope. The black points in the third column represent the locations left by the release of DMTD which indicates a larger and homogeneous release from Epoxy-DMTD/TiOx coatings. Scale bar: 100 μm.

show high levels of stability during cyclic wet/dry re-exposure to 0.05 M NaCl solutions. [30]

In order to study the impact of the TiO_x nanolayer (20 cycles) on the active corrosion inhibition at damaged locations (circular damage with Ø = 1 mm, 200 um penetration into the metal) given by DMTD-loaded coatings, a detailed study under wet/dry cyclic exposure conditions was performed. Herein, a single wet-dry cycle exposure represents a 2 h exposure to 0.05 M NaCl solution followed by a 1 h drying process. The exposure time to electrolyte was determined based on the release kinetics study shown in Fig. 4c wherein most of the inhibitor has been released from the grind coating in the first 2 h of exposure. During a maximum of 3 cycles of exposure, the coating damages were monitored with an in-situ hyphenated electrochemical (electrochemical potential noise) and optical (image reflectometry) home-built setup as described in the experimental section. The electrochemical potential noise (EPN) signals and original optical images at the start and the end of exposure during each cycle are shown in the supporting information Fig. S3. Without post-treatment, the optical images obtained during immersion do not allow differentiation during exposure thereby requiring image processing to extract quantitative information. Hence, the surface activity at the exposed metal and at the surrounding coating matrix are extracted from the optical images by a pixel-by-pixel changes analysis implemented in ImageJ software as described in our previous works. [10,22,30] Fig. 6 and Fig. 7 illustrates the resultant surface global activity maps (GAM) and quantified activity plots for the metal damage site, and local post-mortem images of the damage captured by a confocal microscope for the reference Epoxy coating and DMTD-loaded coatings.

As seen in Fig. 6, an epoxy coating without DMTD rapidly shows the appearance of local activity (within the first minute of exposure) which progresses to a surface area coverage of the damaged location of around 20 % after 2 h exposure. The progression of the local activity is relatively fast and goes from 2.0E-03 % s^{-1} during the first hour to a slightly faster process 3.1E-03 % s^{-1} after 1.5 h exposure (Fig. 8) in good agreement with dealloying at intermetallic particles followed by trenching. [22] The corresponding EPN signal (Fig. S3) can be regarded as typical for the corrosion of AA2024-T3, which shows lots of short transients and ends at -431 mV vs Ag/AgCl, well in line with the corrosion potential of AA2024 at thermodynamic equilibrium after intermetallic particles (IM) dealloying and trenching. [31] These results are in good agreement with the local post-mortem image (Fig. 6b) which shows a large extent of

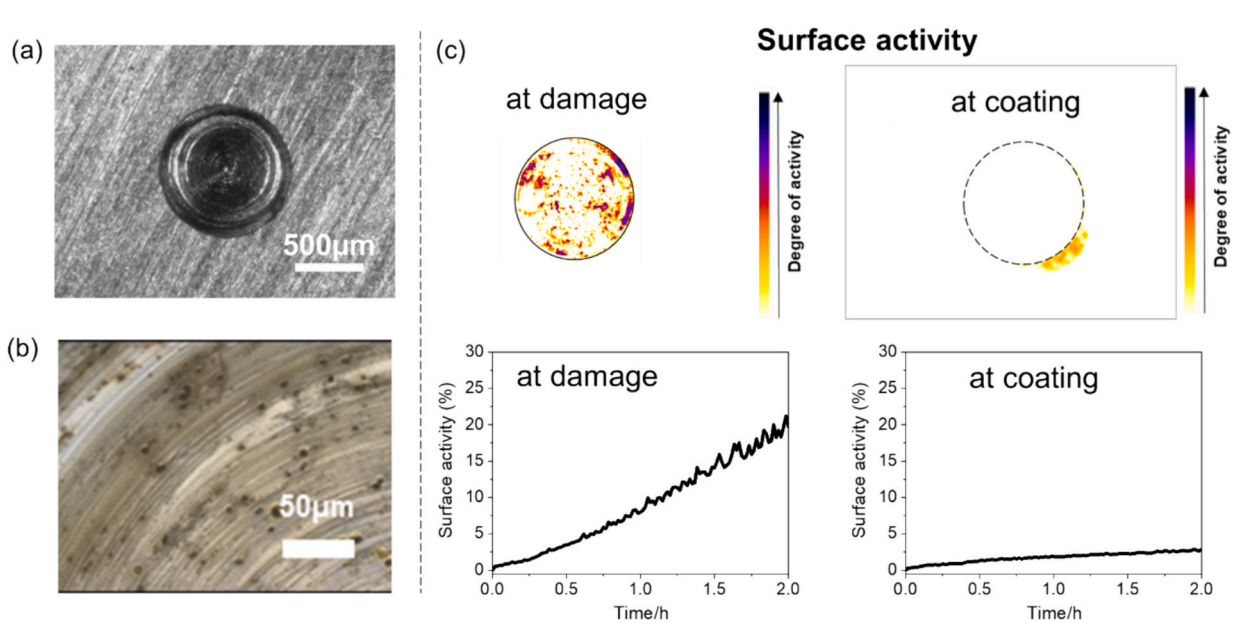

Fig. 6. (a) Optical image, (b) local post-mortem image, and (c) Surface activity plots, activity map at the damage and coating area for damaged Epoxy coating during 2 h exposure in 0.05 M NaCl solution. The diameter of the circle in the activity map is 1 mm. The minimum activity on the coating area indicates there was only coating delamination on this coating.

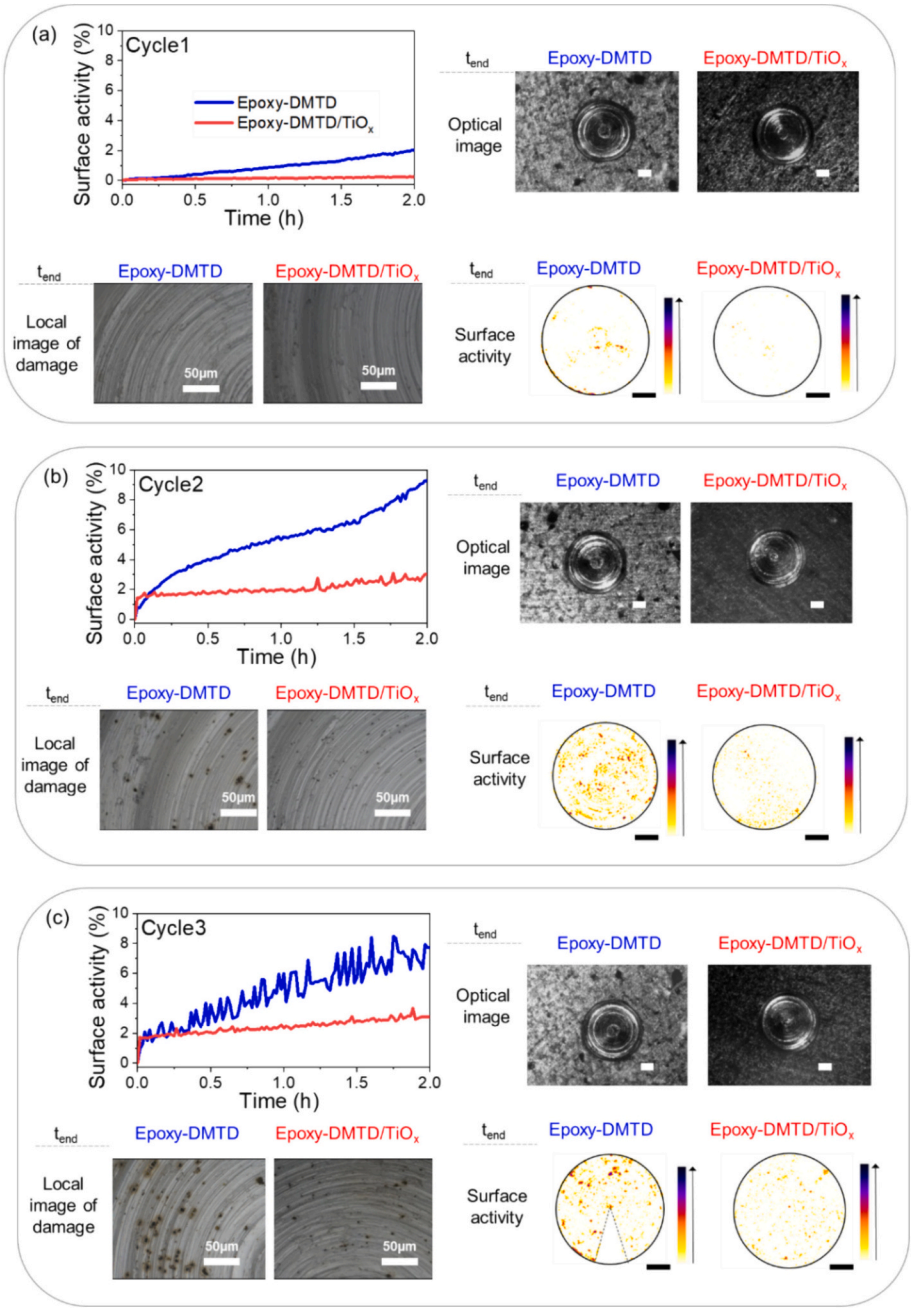

Fig. 7. Figure shows the quantified surface activity plots (left-top), optical images (right-top), local post-mortem images (left-bottom) and global activity maps (GAM; right-bottom) at the exposed metal surface at the damage location at the end of wet-dry cycle 1 (a), cycle 2 (b) and cycle 3 (c) for Epoxy-DMTD (blue) and Epoxy-DMTD/TiO_x (red) coatings. The diameter of the damage hole in the GAMs is 1 mm. The sector with a dashed outline on the activity map of the third cycle (in c) of the Epoxy-DMTD represents a non-quantifiable location due to the presence of an air bubble and has therefore been omitted from the analysis. Scale bars in optical images and activity maps are 200 μm. The color bars in the GAMs show the activity intensity increase where yellow is low intensity and red is high activity. The Epoxy reference showing massive activity is shown in the Fig. 6. The activity maps and plots show the reduction of the local activity (corrosion) when using the organic inhibitors coated with a TiO_x nanolayer. (For interpretation of the references to color in this figure legend, the reader is referred to the web version of this article.)

corrosion within 2 h of exposure (1 cycle).

A different behavior is observed for coatings containing DMTD in the first cycle of exposure. Fig. 7a shows that both Epoxy-DMTD and Epoxy-DMTD/TiO_x coatings exhibit low-level surface activities at the metallic surface (low-intensity corrosion activities at <2 % surface coverage). Additionally, the progression of the surface activity is significantly slower than for the uninhibited system, with Epoxy-DMTD <5.0E-04 % s^{-1} and Epoxy-DMTD/TiO_x one extra order of magnitude slower <7.0E-05 % s^{-1}, as shown in Fig. 8, in good agreement with the local post-mortem images of the damage (Fig. 7a) showing no signs of corrosion (no local dark spots). The EPN of Epoxy-DMTD and Epoxy-DMTD/TiO_x coatings in Fig. S3 are both smooth (no transients) with increase and decrease events and ended with a more negative EPN value (-556 mV and -778 mV respectively) compared with the coating without DMTD. The decrease of the potential and absence of potential transients is a clear indication of the interaction of DMTD at the metallic surface preventing local dealloying. These results indicate DMTD is able to come out from both Epoxy-DMTD and Epoxy-DMTD/TiO_x coatings and

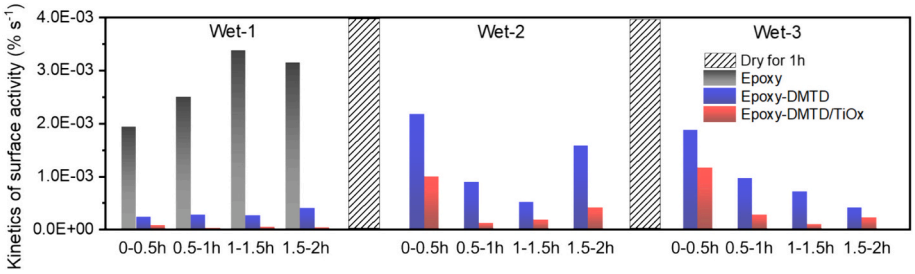

Fig. 8. Surface activity kinetics at the damage every half hour for 1 cycle Epoxy, 3 cycles Epoxy-DMTD and 3 cycles Epoxy-DMTD/TiO_x coatings exposure.

protect the exposed metal area at the first cycle even if in a more efficient manner in the case of the coating containing DMTD coated with a TiO_x nanolayer (Epoxy-DMTD/TiO_x).

Differences between the two inhibited coatings become more obvious during the second cycle (Fig. 7b). The surface activity of Epoxy-DMTD coating at damage shows surface activity propagation kinetics comparable to the uninhibited system (Fig. 7b and Fig. 8): 2.0E-03 % s^{-1} in the first half an hour indicating activation of local degradation, followed by a slowing down of the process to 5.0E-04 % s^{-1} during the subsequent hour likely due to the effect of inhibitor release or inhibiting layer healing, [28] and finally increasing again to 1.5E-03 % s^{-1} as an indication of reactivation of the corrosion process leading to a surface coverage around 9.5 % at the end of the second cycle (Fig. 7b). In very good agreement with this, the EPN signal shows potential noise transients in the initial 1800s (30 min) and turns to smooth signal reaching a potential value of -600 mV (Fig. S3). These findings, together with the post-mortem image showing the presence of some pits and oxides (Fig. 7b), validate the loss of full protection provided by the Epoxy-DMTD coating during the second cycle.

The Epoxy-DMTD/TiO_x coating on the other hand, initially shows a similar surface activity kinetics (Fig. 8, k = 1.0E-03 % s^{-1} during first 30 min) yet rapidly followed by an activity plateau reaching a maximum of 1.7 % surface coverage, still within the boundaries of intermetallic particle surface coverage. [22] The EPN again shows some noise transients in the first 1800s attributed to local dealloying or/and local breakdown of the inhibiting layer followed by a slow smooth decrease indicative of inhibitor repassivation as shown in Fig. S3. The post-mortem image (Fig. 7b) after the second cycle confirms these measurements with minor dealloying at some intermetallic particle sites.

During the third wet-dry cycle, the inhibited Epoxy-DMTD and Epoxy-DMTD/TiO_x coatings show analogous behavior to that shown in cycle 2 in terms of surface activity (Fig. 7c) and EPN signal (Fig. S3). An increasing surface activity with the immersion time observed in the Epoxy-DMTD sample indicates a progression of the local corrosion attack even if still at a slower pace than in the uninhibited coatings. The Epoxy-DMTD/TiO_x coating on the other hand shows again a fast activity during the first half hour of immersion followed by a very slow progression of surface activity and EPN stabilization (Fig. S3, Fig. 8) to reach a remarkably low surface activity coverage below 2 % (Fig. 7c). These results demonstrate the advantageous use of a protective thin nanolayer around the organic corrosion inhibitor to induce sustained and efficient corrosion protection at damaged sites.

3.4. Effect of protective nanolayer on the release mechanism responsible for sustained protection

The above results clearly demonstrate that gas-deposited protective nanolayers on DMTD reduce the negative interaction with the surrounding polymer matrix, improve inhibitor release and enable better corrosion inhibition. To unveil the mechanism that allowed comparable initial corrosion protection behavior in the two inhibited coating systems and clear differences after the first wet-dry cycle a dedicated release-to-protection analysis was made.

In the studied coatings, the corrosion inhibitors have two paths to release and protect the damage: (i) through the path created during water ingress on the coating surface, and (ii) from the sidewalls at the damage location. The contribution of the former is clearly detectable during the wet exposure monitoring and global activity maps of the coating.

Fig. 9a shows the related activity (maps and plots) localized and quantified at the surrounding coating matrix around a damage location at the end of each cycle for Epoxy-DMTD and Epoxy-DMTD/TiO_x coatings. Local activity appears homogeneously distributed on the two coatings surfaces, even though this is more evident, intense and growing in time in the case of the Epoxy-DMTD coating. The low local activity observed for the Epoxy-DMTD/TiO_x coating suggests a low contribution of the exposed top surface to the inhibitor release. This coating activity appears different from the activity reported in our previous work with high pigment volume concentration loading (30 %) where water ingress from the damage walls and subsequent inhibitor dissolution and transport to the damage location appears as local activity rings progressing outwards from the damage location. [10] The absence of such activity rings in this work suggests that in the studied coatings, no clear inter-particle connection paths governing lateral release at the damage location are present, as expected for the relatively low pigment volume concentration used (10 %).

To quantify the DMTD release from the damage wall and from the top surface, UV–Vis release studies with an intact coating and a damaged coating were performed in steps of 2 h as in the wet-dry cyclic testing. Fig. 9b shows an overview of the DMTD release amounts for the Epoxy-DMTD and Epoxy-DMTD/TiO_x from coating and from damage for each cycle. In agreement with the global activity maps (Fig. 9a), for the Epoxy-DMTD coating the majority of the DMTD is released from the coating surface through water diffusion, not from the damaged polymer walls. This is maintained during the three cycles, yet with decreasing DMTD release.

During the first cycle, the Epoxy-DMTD/TiO_x coating released twice the amount of DMTD compared to Epoxy-DMTD, with half of the release coming from the damage coating walls. The same release contribution was observed in the subsequent 2nd and 3rd cycle, yet with lower inhibitor release due to depletion and/or diffusion restrictions.

Fig. 9b shows that in the first cycle, approximately 0.05 mM and 0.1 mM DMTD were released from the Epoxy-DMTD and Epoxy-DMTD/TiO_x coatings, respectively. Inhibitor release in these cases comes from the intact top surface of the coating and the walls of the induced hole. The amount of inhibitor released directly from the intact top surface (around 0.05 mM in both cases) is significantly lower than that for coatings that have been surface damaged by sandpaper grinding as shown in Fig. 4c (with 1.7 mM for Epoxy/DMTD and 2.2 mM for Epoxy-DMTD/TiO_x for a comparable exposure area of 2.5 cm in diameter). Such a release difference confirms the reduced reaction in the case of a protected DMTD with a gas-deposited nanolayer and the higher release for such samples in the presence of damage (i.e. hole in this work). As observed in Fig. 7a, the exposed metal surface at the hole remains protected in both cases in this first exposure cycle. This indicates the inhibitor amounts released are sufficient for corrosion protection. This is confirmed by the results

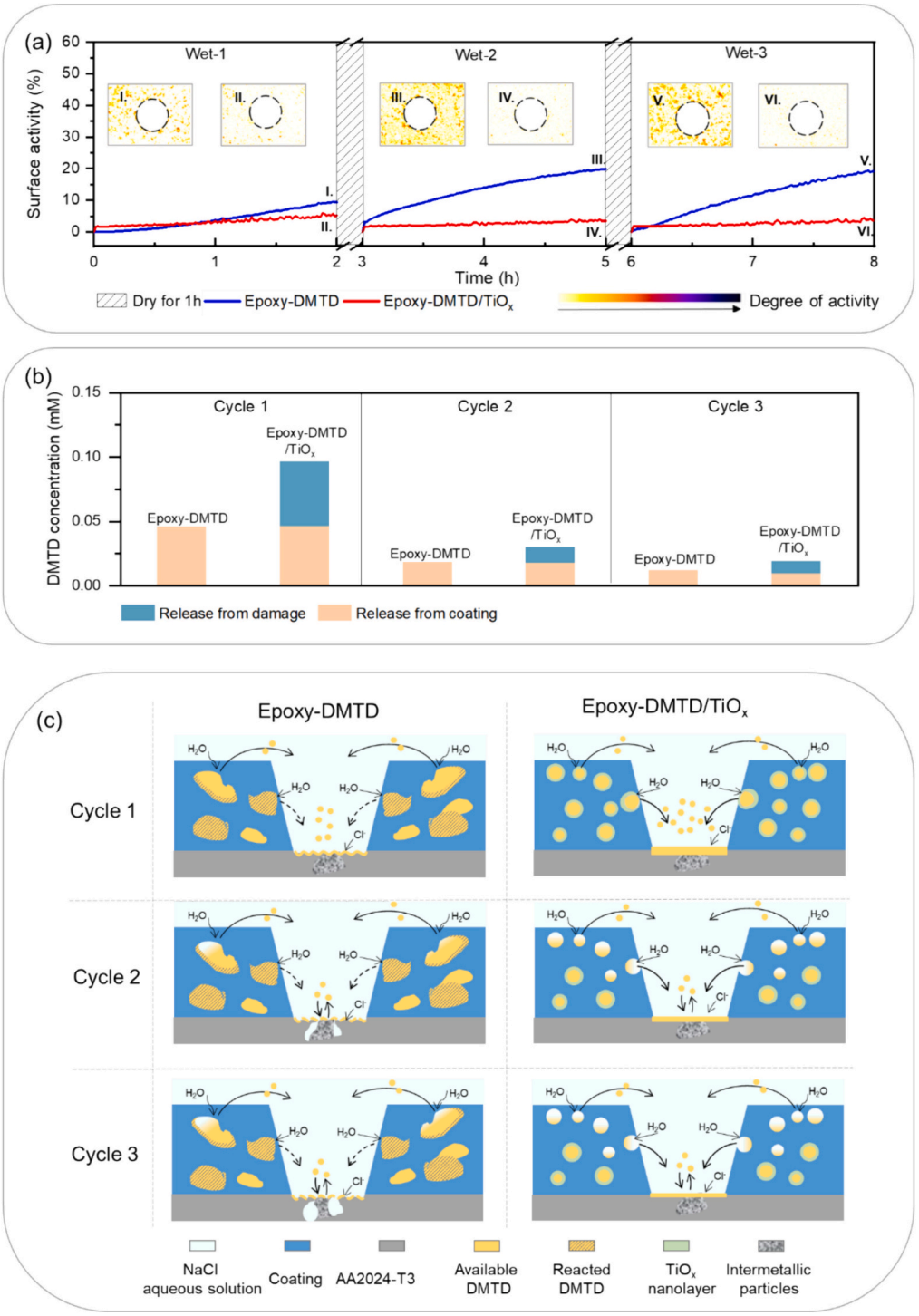

Fig. 9. (a) Surface activity plots and global activity maps at coating areas around a damage location at the end of each cycle for Epoxy-DMTD and Epoxy-DMTD/TiO_x coatings. For each exposure period, fresh 4.5 mL 0.05 M NaCl solution was used. The diameter of circles in activity maps is 1 mm. Figure shows the higher level of homogeneous activity due to water ingress and inhibitor dissolution in the Epoxy-DMTD coating. Despite the lower activity the Epoxy-DMTD/TiO_x coatings showed higher inhibitory effect. (b) Concentrations of DMTD released into 4.5 mL 0.05 M NaCl solution from an intact coating and from a coating with a damage for Epoxy-DMTD and Epoxy-DMTD/TiO_x coatings during 3 cycles; (c) Proposed mechanism for the release of DMTD from Epoxy-DMTD and Epoxy-DMTD/TiO_x coatings, and the stability of corrosion inhibition throughout 3 exposure cycles.

shown in Fig. S4 demonstrating that the minimum required concentration of DMTD in the electrolyte to protect a Ø = 1 mm damage on an Epoxy coating is 0.05 mM.

In the second and third cycle, the Epoxy-DMTD coating exhibited some dealloying and trenching on the intermetallic particles as shown in Fig. 7b, whereas Epoxy-DMTD/TiO_x coating did not display any significant signs of corrosion. During the second cycle, roughly 0.02 mM of DMTD was released from Epoxy-DMTD, and 0.03 mM was released from Epoxy-DMTD/TiO_x coating. Even a bit less during cycle 3. As shown in Fig. S4, the damage on an Epoxy coating can be protected with at least 0.05 mM in 0.05 M NaCl solution. However, once the samples were re-exposed to a fresh 0.05 M NaCl solution without DMTD, only the

sample pre-exposed to 0.1 mM DMTD solution did not show any sign of corrosion (Fig. S4, second column), indicating a higher inhibiting layer stability. This supports the idea that despite the inhibitor release for the Epoxy-DMTD/TiO_x coating in the second and third cycles being below protection levels, the surface is still protected due to a higher stability of the inhibiting layer created at a 0.1 mM concentration during the first cycle and the extra inhibitor released from the coating. These results support the idea demonstrated in our previous work [30] that finding methods to make the inhibiting layer more stable can contribute to the development of more efficient anti-corrosion systems, even when the inhibitor supply from the coating is reduced in time. Moreover, the continuous release at the second and third cycles is also beneficial for keeping the stability of the DMTD layer.

Fig. 9c schematizes the release and protection at damaged sites in the absence of a protective nanolayer (Epoxy-DMTD) and in the presence of a gas-phase deposited nanolayer around the DMTD (Epoxy-DMTD/TiO_x). Supporting Information Fig. S5 presents the cross-sectional micrographs of both coatings. The cross-section images reveal an enhanced dispersion of inhibitor particles due to the protective nanolayer, consistent with what is observed in the top view of the coatings shown in Fig. 1. Fig. 9c illustrates how the nanolayer allows a better homogeneous particle dispersion, with a higher content of available DMTD inhibitor due to reduced reaction with the surrounding matrix that in turn allows for fast formation of stable inhibiting layers and sustained release of corrosion inhibitors to allow for sustained local corrosion protection.

4. Conclusions

In this work, gas-phase deposition in a fluidized bed reactor is presented as a method to modify the surface of organic corrosion inhibitor particles to prevent their interaction with the epoxy-amine coating matrix. TEM of surface-modified inhibitor particles confirms the deposition of a nano-thin TiO_x layer on the surface of DMTD particles. The modified particles were incorporated in highly reactive epoxy-amine coatings. Optical images, thermal analysis and release tests show that a 20 nm nanolayer can effectively improve the particle dispersion and reduce the reaction between DMTD and epoxy-amine matrix. Furthermore, the effect of the nanolayer on the corrosion protection of damaged coating locations exposed to wet/dry cycles was evaluated by in-situ optical-electrochemical tests. The local image reflectometry coupled with electrochemical potential noise and release tests demonstrated that using a gas phase deposited nanolayer around the organic microparticles, not only improves dispersion but improves inhibitor release and efficient long-term protection at damaged locations exposed to wet-wash-dry cycles. The results highlight the importance of sufficient release from the damage sites at the first cycle to (i) offer direct protection but also (ii) stable inhibiting layers during reimmersion, a new paradigm in corrosion protection with inhibitors.

Overall, this work specifically tackles the enduring challenge of incorporating effective organic corrosion inhibitors into organic coatings without triggering unwanted reactions and paves the way for utilizing highly reactive yet functional organic particles with functions such as corrosion inhibition, painkilling, sensing, antifouling, antibacterial, or luminescence in polymers across a wide array of applications. Although these initial results are promising, there is a wealth of potential for further improvements in organic particle selection, nanolayer composition, cycle optimization, and specific process parameters. Furthermore, while gas-phase deposition demonstrates potential in controlling inhibitor release and enhancing coating properties and effectiveness through precise deposition layer growth, it requires further refinement compared to traditional wet chemistry methods, particularly in terms of reducing process complexity, enhancing cost-efficiency, and scaling up.

CRediT authorship contribution statement

Jingjing Zhao: Writing – original draft, Visualization, Validation, Methodology, Investigation, Formal analysis, Data curation, Conceptualization. **J. Ruud van Ommen:** Writing – review & editing, Supervision, Resources, Methodology, Conceptualization. **Santiago J. Garcia:** Writing – review & editing, Writing – original draft, Visualization, Validation, Supervision, Resources, Project administration, Methodology, Investigation, Funding acquisition, Formal analysis, Conceptualization.

Declaration of competing interest

There are no conflicts to declare.

Data availability

The data underlying this article are openly available at https://doi.org/10.4121/83c5e0f7-9aab-40f5-983a-cd08a2eefb7c.

Acknowledgements

The authors acknowledge the financial support by Airbus Operations GmbH and Holland High Tech program. The authors acknowledge Dr. Markus Jordan from Airbus Operations GmbH for his continued support and constructive discussions, Mr. Albert Santoso, Mr. Rens Kamphorst and Mr. Bart Boshuizen for their support with the gas-phase deposition set-up and XPS analysis, Mr. Marlon Mopon for his support with the opto-electrochemical set-up, Mr. Tinashe Darikwa for the DSC measurements, Mr. Frans Tichelaar for the TEM measurements, and Dr. Peter Visser from AkzoNobel for supplying the epoxy/amine resins.

Appendix A. Supplementary data

Supplementary data to this article can be found online at https://doi.org/10.1016/j.porgcoat.2024.108522.

References

[1] G. Williams, A.J. Coleman, H.N. McMurray, Inhibition of aluminium alloy AA2024-T3 pitting corrosion by copper complexing compounds, Electrochim. Acta 55 (2010) 5947–5958, https://doi.org/10.1016/j.electacta.2010.05.049.
[2] K.A. Yasakau, M.L. Zheludkevich, S.V. Lamaka, M.G. Ferreira, Mechanism of corrosion inhibition of AA2024 by rare-earth compounds, J. Phys. Chem. B 110 (2006) 5515–5528, https://doi.org/10.1021/jp0560664.
[3] T.G. Harvey, S.G. Hardin, A.E. Hughes, T.H. Muster, P.A. White, T.A. Markley, P. A. Corrigan, J. Mardel, S.J. Garcia, J.M.C. Mol, A.M. Glenn, The effect of inhibitor structure on the corrosion of AA2024 and AA707, Corros. Sci. 53 (2011) 2184–2190, https://doi.org/10.1016/j.corsci.2011.02.040.
[4] M. Soleymanibrojeni, H. Shi, I.I. Udoh, F. Liu, E.H. Han, Microcontainers with 3-amino-1, 2, 4-triazole-5-thiol for enhancing anticorrosion waterborne coatings for AA2024-T3, Prog. Org. Coat. 137 (2019) 105336, https://doi.org/10.1016/j.porgcoat.2019.105336.
[5] S.R. White, N.R. Sottos, P.H. Geubelle, J.S. Moore, M.R. Kessler, S. Sriram, E. N. Brown, S. Viswanathan, Autonomic healing of polymer composites, Nature 409 (2001) 794–797, https://doi.org/10.1038/35057232.
[6] A. Yabuki, T. Shiraiwa, I.W. Fathona, pH-controlled self-healing polymer coatings with cellulose nanofibers providing an effective release of corrosion inhibitor, Corros. Sci. 103 (2016) 117–123, https://doi.org/10.1016/j.corsci.2015.11.015.
[7] E.L. Ferrer, A.P. Rollon, H.D. Mendoza, U. Lafont, S.J. Garcia, Double-doped zeolites for corrosion protection of aluminium alloys, Microporous Mesoporous Mater. 188 (2014) 8–15, https://doi.org/10.1016/j.micromeso.2014.01.004.
[8] D. Fix, D.V. Andreeva, Y.M. Lvov, D.G. Shchukin, H. Möhwald, Application of inhibitor-loaded halloysite nanotubes in active anti-corrosive coatings, Adv. Funct. Mater. 19 (2009) 1720, https://doi.org/10.1002/adfm.200800946.
[9] C. Li, X. Guo, G.S. Frankel, Corrosion inhibition of AA2024-T3 by a coating containing dual-pH sensitive, corrosion inhibitor loaded microspheres, Corros. Sci. 192 (2021) 109835, https://doi.org/10.1016/j.corsci.2021.109835.
[10] P.J. Denissen, A.M. Homborg, S.J. Garcia, Requirements for corrosion inhibitor release from damaged primers for stable protection: a simulation and experimental approach using cerium loaded carriers, Surf. Coat. Technol. 430 (2022) 127966, https://doi.org/10.1016/j.surfcoat.2021.127966.
[11] R. Raj, Y. Morozov, L.M. Calado, M.G. Taryba, R. Kahraman, R.A. Shakoor, M. F. Montemor, Calcium carbonate particles loaded with triethanolamine and

polyethylenimine for enhanced corrosion protection of epoxy coated steel, Corros. Sci. 167 (2020) 108548, https://doi.org/10.1016/j.corsci.2020.108548.
[12] M. Knez, K. Nielsch, L. Niinistö, Synthesis and surface engineering of complex nanostructures by atomic layer deposition, Adv. Mater. 19 (2007) 3425–3438, https://doi.org/10.1002/adma.200700079.
[13] R.H. Vervuurt, W.M. Kessels, A.A. Bol, Atomic layer deposition for graphene device integration, Adv. Mater. Interfaces 4 (2017) 1700232, https://doi.org/10.1002/admi.201700232.
[14] S.T. Zhang, A. Maltseva, G. Herting, J.F. Guillemoles, N. Schneider, I. Odnevall, P. Volovitch, Importance of atmospheric aerosol pollutants on the degradation of Al2O3 encapsulated Al-doped zinc oxide window layers in solar cells, Prog. Photovolt. Res. Appl. 30 (2022) 552–566, https://doi.org/10.1002/pip.3527.
[15] T.O. Kääriäinen, M. Kemell, M. Vehkamäki, M.L. Kääriäinen, A. Correia, H. A. Santos, L.M. Bimbo, J. Hirvonen, P. Hoppu, S.M. George, D.C. Cameron, M. Ritala, M. Leskelä, Surface modification of acetaminophen particles by atomic layer deposition, Int. J. Pharm. 525 (2017) 160–174, https://doi.org/10.1016/j.ijpharm.2017.04.031.
[16] D. La Zara, F. Zhang, F. Sun, M.R. Bailey, M.J. Quayle, G. Petersson, S. Folestad, J. R. van Ommen, Drug powders with tunable wettability by atomic and molecular layer deposition: from highly hydrophilic to superhydrophobic, Appl. Mater. Today 22 (2021) 100945, https://doi.org/10.1016/j.apmt.2021.100945.
[17] D. La Zara, F. Sun, F. Zhang, F. Franek, K.B. Sivars, J. Horndahl, S. Bates, M. Brännström, P. Ewing, M.J. Quayle, G. Petersson, S. Folestad, J.R. van Ommen, Controlled pulmonary delivery of carrier-free budesonide dry powder by atomic layer deposition, ACS Nano 15 (2021) 6684–6698, https://doi.org/10.1021/acsnano.0c10040.
[18] S. Gupta, M. Mittal, A.S. Rathore, Atomic layer deposition coating on the surface of active pharmaceutical ingredients to reduce surface charge build-up, ACS Appl. Mater. Interfaces 14 (2022) 27195–27202, https://doi.org/10.1021/acsami.2c05761.
[19] F. Zhang, K. Wu, D. La Zara, F. Sun, M.J. Quayle, G. Petersson, S. Folestad, J. Wei Chew, J.R. van Ommen, Tailoring the flow properties of inhaled micronized drug powders by atomic and molecular layer deposition, Chem. Eng. J. 462 (2023) 142131, https://doi.org/10.1016/j.cej.2023.142131.
[20] D. Zhang, J.H. Flory, S. Panmai, U. Batra, M.J. Kaufman, Wettability of pharmaceutical solids: its measurement and influence on wet granulation, Colloids Surf. A Physicochem. Eng. Asp. 206 (2002) 547–554, https://doi.org/10.1016/S0927-7757(02)00091-2.
[21] C.L.N. Vo, C. Park, B.J. Lee, Current trends and future perspectives of solid dispersions containing poorly water-soluble drugs, Eur. J. Pharm. Biopharm. 85 (2013) 799–813, https://doi.org/10.1016/j.ejpb.2013.09.007.
[22] M. Olgiati, P.J. Denissen, S.J. Garcia, When all intermetallics dealloy in AA2024-T3: quantifying early stage intermetallic corrosion kinetics under immersion, Corros. Sci. 192 (2021) 109836, https://doi.org/10.1016/j.corsci.2021.109836.
[23] J.A. Carioscia, J.W. Stansbury, C.N. Bowman, Evaluation and control of thiol–ene/thiol–epoxy hybrid networks, Polymer 48 (2007) 1526–1532, https://doi.org/10.1016/j.polymer.2007.01.044.
[24] J.W. Chan, C.E. Hoyle, A.B. Lowe, M. Bowman, Nucleophile-initiated thiol-Michael reactions: effect of organocatalyst, thiol, and ene, Macromolecules 43 (2010) 6381–6388, https://doi.org/10.1021/ma101069c.
[25] A.O. Konuray, X. Fernandez-Francos, X. Ramis, Latent curing of epoxy-thiol thermosets, Polymer 116 (2017) 191–203, https://doi.org/10.1016/j.polymer.2017.03.064.
[26] M.C. Biesinger, L.W. Lau, A.R. Gerson, R.S.C. Smart, Resolving surface chemical states in XPS analysis of first row transition metals, oxides and hydroxides: Cr, Mn, Fe, Co and Ni, Appl. Surf. Sci. 257 (2011) 2717–2730, https://doi.org/10.1016/j.apsusc.2010.10.051.
[27] D.G. Castner, K. Hinds, D.W. Grainger, X-ray photoelectron spectroscopy sulfur 2p study of organic thiol and disulfide binding interactions with gold surfaces, Langmuir 12 (1996) 5083–5086, https://doi.org/10.1021/la960465w.
[28] S.V. Levchik, E.D. Weil, Thermal decomposition, combustion and flame-retardancy of epoxy resins-a review of the recent literature, Polym. Int. 53 (2004) 1901–1929, https://doi.org/10.1002/pi.1473.
[29] A.E. Hughes, I.S. Cole, T.H. Muster, R.J. Varley, Designing green, self-healing coatings for metal protection, NPG Asia Mater. 2 (2010) 143–151, https://doi.org/10.1038/asiamat.2010.136.
[30] J. Zhao, A. Santoso, S.J. Garcia, Small concentrations of NaCl help building stable inhibiting layers from 2, 5-dimercapto-1, 3, 4-thiadiazole (DMTD) on AA2024-T3, Corros. Sci. 225 (2023) 111562, https://doi.org/10.1016/j.corsci.2023.111562.
[31] A.T.N. Tita, J.C. Hauth, A. Grimes, J. Owen, A. Stamm, W. Andrews, Decreasing incidence of postcesarean endometritis with extended-spectrum antibiotic prophylaxis, Obstet. Gynecol. 111 (2008) 51–56, https://doi.org/10.1097/01.AOG.0000295868.43851.39.